Influence of the stacking sequence on layered-chalcogenide properties: first principles investigation of Pb 2 Bi 2 Te 5

Weiliang Ma, M. -C. Record, Jing Tian, P. Boulet

Influence of the stacking sequence on layered-chalcogenides properties: First principle investigation of $Pb_2Bi_2Te_5$

Weiliang MA,[ab] Marie-Christine RECORD,*[a] Jing TIAN,[ab] and Pascal BOULET[b]

ABSTRACT: The $Pb_2Bi_2Te_5$ compound has been reported in literature with two stacking sequences -Te-Pb-Te-Bi-Te-Bi-Te-Pb-Te- and -Te-Bi-Te-Pb-Te-Pb-Te-Bi-Te- labelled in this work as A and B, respectively. The electronic and the thermoelectric properties of the $Pb_2Bi_2Te_5$ compound with the 2 different stacking sequences have been determined from a series of first principles calculations using density functional theory (DFT). The related compounds PbTe and Bi_2Te_3 have also been investigated for comparison. Different exchange-correlation functionals have been tested, w/o spin-orbit coupling, which has been found to have important effects. The elastic moduli, dielectric constants, Born effective charges, and phonon dispersion within the quasi-harmonic approximation have also been calculated and based on these calculations results, the thermal conductivity has been determined by solving the Boltzmann transport equation. Additionally, the QTAIM theory was employed to explain the differences in the properties of the 2 stackings. The most interesting compound for thermoelectric applications has been found to be $Pb_2Bi_2Te_5$ with the stacking B sequence. The highest zT values have been found to be 4.02 in the *a*-axis direction and 2.26 in the *c*-axis one.

1 Introduction

Due to their low lattice heat conductivity, complex layered chalcogenides such as ternary compounds in the quasi-binary $A^{IV}C^{VI}$-$B_2^VC_3^{VI}$ systems (A^{IV} = Ge, Sn, Pb; B_V = Bi, Sb ; C_{VI} = Te, Se) are potential candidates for thermoelectric applications.[1] The existence of homologous series of layered compounds of the n($A^{IV}C^{VI}$)-m($B_2^VC_3^{VI}$) type in this system[2] offers large possibilities for optimizing the thermoelectric properties. Indeed by using different types of stacks as well as various combinations, these homologous series behave as compounds generating devices. Many n($A^{IV}C^{VI}$)-m($B_2^VC_3^{VI}$) compounds have been already investigated as potential thermoelectric materials[3–6], phase change memories for optical data storage[6,7] and topological insulators (TIs)[8–16].

In the PbTe-Bi_2Te_3 quasi-binary system, six ternary compounds belonging to the homologous series n($A^{IV}C^{VI}$)-m($B_2^VC_3^{VI}$) have been evidenced. Five of them, namely $PbBi_2Te_4$, $Pb_2Bi_6Te_{11}$, $PbBi_4Te_7$, $PbBi_6Te_{10}$, and $PbBi_8Te_{13}$ with a trigonal symmetry, are located in the Bi_2Te_3 rich side[17–19], whereas $Pb_2Bi_2Te_5$ with a nine-layers hexagonal unit cell[18,20] is located in the PbTe rich side. Most of the studies reported in literature concerns the compounds belonging to the Bi_2Te_3 rich side, e.g. thermodynamic properties of $PbBi_4Te_7$ and $PbBi_2Te_4$[21], vibrational spectra of $Pb_2Bi_2Te_3$, $PbBi_2Te_4$ and $PbBi_4Te_7$[22], thermoelectric properties of $PbBi_2Te_4$[4] and $PbBi_4Te_7$[23].

The $Pb_2Bi_2Te_5$ compound with a stability that was even questioned[17] has been much less investigated. In 1969, Petrov et al.[18] synthesized $Pb_2Bi_2Te_5$ from $PbBi_4Te_7$ using a long time annealing to evaporate Bi_2Te_3 and characterized it by electronography. The unit cell of $Pb_2Bi_2Te_5$ consists in nine-atomic layers, which are made by inserting two PbTe into Bi_2Te_3 according to the following sequence: -Te-Pb-Te-Bi-Te-Bi-Te-Pb-Te-, whereas the unit cell of $PbBi_4Te_7$ consists in 12-atomic layers made of a 5-layers slab (-Te-Bi-Te-Bi-Te-) and a 7-layers slab (-Te-Bi-Te-Pb-Te-Bi-Te-). The nine atomic layers in $Pb_2Bi_2Te_5$ are linked by van der Waals interactions. Recently Chartterjee et al.[20] synthesized by a simple solution-phase method at low temperatures a two-dimensional $Pb_2Bi_2Te_5$ nano-sheet and characterized it by several methods including powder X-ray diffraction, inductively coupled plasma atomic emission spectroscopy (ICP-AES) and energy dispersive X-ray analysis (EDAX). In agreement with the previous results[18], the unit cell of $Pb_2Bi_2Te_5$ is constituted of nine-atomic layers but with a different atomic sequence, namely –Te-Bi-Te-Pb-Te-Pb-Te-Bi-Te-.

Therefore the stability and the atomic layer stacking sequence for this compound are still questioned.

In the present work, by using first principles calculations and density functional perturbation theory (DFPT), we investigated the stability, the electronic structure, the thermoelectric properties and the thermal conductivity of $Pb_2Bi_2Te_5$ for each stacking sequence.

2 Computational procedure

The electronic structure calculations have been performed within the frame of density functional theory using all-electron FP-LAPW approach with local orbital method as implemented in WIEN2K[24]. Several exchange-correlation functionals have been used the detail of which will be mentioned when appropriate in the results section. For structural optimizations the Brillouin zone has been sampled with the k-meshes $8 \times 8 \times 8$, $8 \times 8 \times 8$ and $12 \times 12 \times 2$, for PbTe,

[0a] *Aix-Marseille University, University of Toulon, CNRS, IM2NP, Marseille, France. E-mail: weiliang.ma@etu.univ-amu.fr, Corresponding author: m-c.record@univ-amu.fr*

[0b] *Aix-Marseille University, CNRS, MADIREL, Marseille, France. E-mail: jing.tian@etu.univ-amu.fr, pascal.boulet@univ-amu.fr*

Bi_2Te_3 and $Pb_2Bi_2Te_5$, respectively. For the subsequent convergence of the self-consistent energy the k-meshes have been set as 16 × 16×16, 16 × 16 × 16 and 18 × 18 × 4. The total energy and atomic forces convergence threshold have been defined as 0.136 meV and 0.257 meV/Å, respectively. The cut off energy for the core-valence separation has been fixed at -5.0 Ry for PbTe and $Pb_2Bi_2Te_5$, and -6.0 Ry for Bi_2Te_3 and the $R_{mt}K_{max}$ value as 9.0. The structure and charge density calculated above are used to analyze the topological properties within QTAIM theory[25,26].

The thermoelectric properties have been computed by solving the Boltzmann transport equation within the constant relaxation time τ and the rigid band structure approximations as implemented in BoltzTraP2 package[27]. The implementation of BoltzTraP2 is based on the use of full bands structure in the Brillouin zone. The sampling, which is important in transport calculation, has been done using a very dense k-mesh of 48 × 48 × 48 for PbTe, 36 × 36 × 36 for Bi_2Te_3, and 64 × 64 × 14 for $Pb_2Bi_2Te_5$. Within the limit of validity of the semi-classical linearized Boltzmann transport equation, the strongly band structure dependent Seebeck coefficient (S) can be directly obtained. By contrast, for the calculation of the electronic part κ_e of the thermal conductivity and the electronic conductivity σ that depend on τ, the τ value has to be evaluated independently. For this, we have used the effective mass approximation with deformation potential (DP) theory to calculate.[28]

Second and third order anharmonic force constants have been calculated by means of DFPT method[29] by using the QUANTUM-ESPRESSO package[30] together with the Phono3py[31] program. A plane-wave energy cutoff of 70 Ry (952 eV) has been employed. Total energies have been minimized with a convergence criterium of 10^{-7} Ry and a total force threshold of 10^{-4} Ry/Bohr. A supercell of 2 × 2 × 2 has been considered, which consists in a total of 64, 40, and 72 atoms for PbTe, Bi_2Te_3 and $Pb_2Bi_2Te_5$, respectively, with 4 × 4 × 4, 6 × 6 × 6 and 4 × 4 × 1 q-mesh sampling. In subsequent post-processing, phonon lifetimes have been sampled with a finer 19 × 19 × 5 mesh.

3 Structural information

The bulk crystal structure of PbTe is a face-centered cubic one (space group $Fm\bar{3}m$) with 2 atoms in the primitive cell (Fig. 1a). Bi_2Te_3 crystallizes in the rhombohedral lattice system ($R\bar{3}m$) with 5 atoms in the primitive cell stacked along the c-axis and can also be described with a hexagonal unit cell (Fig. 1b). There are three equivalent atomic positions, which locate at Bi (μ, μ, μ), Te1 (ν, ν, ν) and Te2 (0, 0, 0). The structure of Bi_2Te_3 consisting in three slabs containing five atom layers each can be easily visualized in the conventional hexagonal cell. The weak Te-Te bonds (373.3 pm[32]) show that adjacent slabs are linked together through van der Waals forces that contribute to the crystal cohesion.

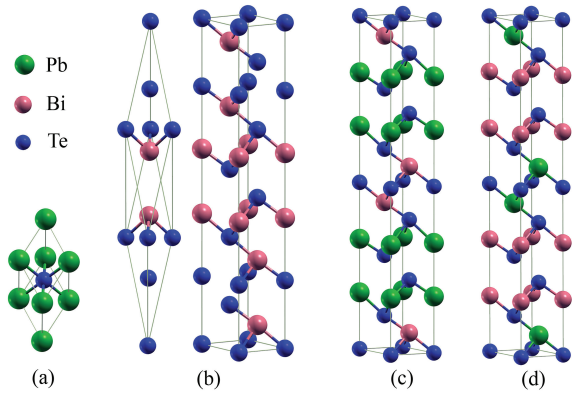

Figure 1 (a) Primitive cell of PbTe; (b) primitive and conventional cells of Bi_2Te_3; (c) 1 × 1 × 2 supercell of $Pb_2Bi_2Te_5$ in stacking A; (d) 1 × 1 × 2 supercell of $Pb_2Bi_2Te_5$ in stacking B.

The studied compound $Pb_2Bi_2Te_5$, which can also be identified as the quasi-binary compound 2(PbTe)-Bi_2Te_3, crystallizes in the P3m1 space group with nine atoms per unit cell stacked along the c-axis. To get a direct view of the atoms stacking, a 1 × 1 × 2 supercell along the c-axis can be considered (see Fig. 1c,d). Among the nine atoms, five inequivalent atoms can be seen. As with Bi_2Te_3 a weak Te-Te interaction is observed between slabs. As mentioned above, two possible atoms sequences have been reported in the literature[18,20]: -Te3-Pb-Te2-Bi-Te1-Bi-Te2-Pb-Te3- (stacking A) and -Te3-Bi-Te2-Pb-Te1-Pb-Te2-Bi-Te3- (stacking B); from one structure to the next the bismuth atoms and the lead ones are interchanged.

4 Results

4.1 Structural properties

The equilibrium lattice constants of PbTe, Bi_2Te_3 and $Pb_2Bi_2Te_5$ have been calculated with three exchange-correlation functionals, namely LDA[33,34], PBE[35], and rev-vdW-DF2[36] with and without spin-orbit coupling (SOC). As there are weak Te-Te bonds in Bi_2Te_3 and $Pb_2Bi_2Te_5$, van der Waals forces have been considered in these compounds. The

rev-vdW-DF2[36] has been shown to be accurate in weakly bound solid systems, such as rare gases and graphite-like structure, and also reliable in strongly bound systems.[37] The calculated lattice constants have been determined by fitting the Birch-Murnaghan equation and the results are listed in Table1 together with experimental data for comparison. Although the calculations on Bi_2Te_3 have been performed with the rhombohedral primitive cell, in order to be consistent with the hexagonal structure of $Pb_2Bi_2Te_5$ we have given in Table 1 the hexagonal lattice parameters of Bi_2Te_3. The effect of SOC on the lattice constants is negligible as we can see from Fig. S1-4 (supplementary materials). For PbTe, the lattice constants are in better agreement with the experimental ones when calculated with PBE, whereas the agreement is better when calculated with rev-vdW-DF2 for Bi_2Te_3. The agreement is also better when using rev-vdW-DF2 for $Pb_2Bi_2Te_5$ stacking B. For $Pb_2Bi_2Te_5$ stacking A from PBE to rev-vdW-DF2 the c lattice parameter agreement is worsen whereas the a one is improved. This could suggest that the contribution of the van der Waals interactions is larger in stacking B. To allow for comparisons between forthcoming results on stacking A and B, the calculations have been performed with the rev-vdW-DF2 functional.

Table 1 Calculated lattice constants in pm and atomic position of fractional coordinates compared with experimental values. The first atomic position is 0 for Te2 in Bi_2Te_3, Te1 in $Pb_2Bi_2Te_5$ for both stacking A and stacking B.

		LDA	PBE	rev-vdW-DF2	Other works
PbTe	*a*	638.4	657.2	-	645.4[38]
Bi_2Te_3	*a*	436.0	445.7	435.0	437[32], 438[39]
	c	2999.9	3074.7	3020.8	3034[32], 3049[39]
	ν	0.209	0.211	0.208	0.212
	μ	0.400	0.399	0.400	0.400
$Pb_2Bi_2Te_5$ stacking A	*a*	443.0	454.4	451.6	446[18]
	c	1687.8	1733.4	1721.1	1752[18]
	Bi	0.1128	0.1117	0.1125	0.109
	Te2	0.2110	0.2066	0.2088	0.218
	Pb	0.3391	0.3394	0.3396	0.329
	Te3	0.4315	0.4293	0.4301	0.440
$Pb_2Bi_2Te_5$ stacking B	*a*	442.8	454.6	450.8	442[20]*
	c	1732.0	1740.8	1768.7	1786[20]*
	Pb	0.1099	0.1097	0.1100	
	Te2	0.2192	0.2194	0.2189	
	Bi	0.3326	0.3349	0.3323	
	Te3	0.4299	0.4294	0.4261	

* Lattice parameter from thin film.

4.2 Electronic and thermal properties

4.2.1 Electronic band structure

Based on the rev-vdW-DF2 optimized structure, the band gaps have been calculated with six different functionals with and without SOC. The Engel-Vosko functional (EV-GGA)[40] allows for reproducing the real exchange potential and the Tran-Blaha-modified Becke-Johnson exchange potential (TB-mBJ)[41] for getting band gaps with a high accuracy similar to that obtained from GW calculations. The HSE hybrid functional, with 25% Hartree-Fock exchange, obviates the band-gap underestimation commonly observed with conventional GGA functionals. The results are presented together with literature values in Table 2. As can be seen, the effect of SOC is significant for all the compounds. The non-SOC energy gaps are overestimated compared with the experimental values. The inclusion of SOC yields closer values to experimental ones, in particular with the PBE functional. Hence this functional has been chosen for all subsequent calculations. Even if gaps are enlarged with HSE, it is still closed for $Pb_2Bi_2Te_5$ with stacking A, which reflects its metallic character. The band gap of $Pb_2Bi_2Te_5$ stacking B is about 0.113 eV, thus this structure can be considered as a narrow gap semiconductor. The gaps of Bi_2Te_3 and $Pb_2Bi_2Te_5$ calculated with and without vdW corrections are close, which indicates that the effect of vdW on their electronic structures is negligible.

The calculated bands structures with and without SOC along high symmetry points of the first Brillouin zone are shown in Figure 2 for PbTe and Bi_2Te_3, and in Figure 3 for $Pb_2Bi_2Te_5$. All the compounds are found to be semiconductors, except $Pb_2Bi_2Te_5$ in stacking A, which shows typical metallic character with overlapping between conduction and valence bands. The valence band maximum (VBM) and conduction band minimum (CBM) for PbTe, Bi_2Te_3 and $Pb_2Bi_2Te_5$ stacking B locate at the Γ point with non-SOC calculations. For Bi_2Te_3 and stacking B the location of both the VBM and CBM differs with and without SOC. Both structures bear a direct and indirect gap without and with SOC, respectively. For Bi_2Te_3 with SOC the VBM locates near the Z point and the CBM is along the Z-F direction with relatively flat bands. For all the compounds, one can observe that SOC splits both high-lying conduction band degenerated orbitals and low-lying valence band ones at high symmetry points. For $Pb_2Bi_2Te_5$, SOC affects more markedly the bottom conduction orbitals than the top valence ones. Therefore the changes in thermoelectric properties should be more noticeable for the *n*-type doped compound. In addition without SOC the bottom conduction orbital

Table 2 Band gaps (eV) for PbTe, Bi_2Te_3, $Pb_2Bi_2Te_5$ stacking A and $Pb_2Bi_2Te_5$ stacking B calculated with various functionals compared to the experimental ones. Both the non-SOC and SOC results (in parenthesis) are presented.

	LDA	PBE	EV	TB-mBJ	PBE/vdw	HSE (this work)	HSE (from lit.)	Exp.
PbTe	0.574	0.827	1.149	1.196	–	1.26	1.13 [42]	0.1941 [43]
	(0.084)	(0.172)	(0.358)	(0.441)	–	(0.379)	(0.29) [42]	
Bi_2Te_3	0.168	0.256	0.521	0.554	0.316	0.633	–	0.1658 [16]
	(0.088)	(0.113)	(0.116)	(0.126)	(0.114)	(0.306)	(0.311) [44]	
$Pb_2Bi_2Te_5$ stacking A	0	0	0	0	0	0	–	–
	(0)	(0)	(0)	(0)	(0)	(0)		
$Pb_2Bi_2Te_5$ stacking B	0.380	0.504	0.766	0.785	0.489	0.887	–	–
	(0.145)	(0.113)	(0.072)	(0.07)	(0.116)	(0.110)		

exhibits a typical parabolic behaviour around the point whereas with SOC the band is flat and extends itself between and A. In the latter case, the band effective mass and electron mobility should then be lighter and higher, respectively, both leading to lower Seebeck coefficient and to higher electrical conductivity. From these effects, coupled with the fact that the gap is significantly lowered by SOC, and assuming that the thermal conductivity is not affected, the zT value for *n*-type $Pb_2Bi_2Te_5$ should be degraded when considering the SOC effect in the calculations and all the more that the temperature increases. These assumptions have been verified by additional calculations (see Fig.S5 in supplementary materials).

Since the effect of SOC on the band structures is significant for all the compounds, except in very few cases where notified, we have included this effect in the following electronic calculations.

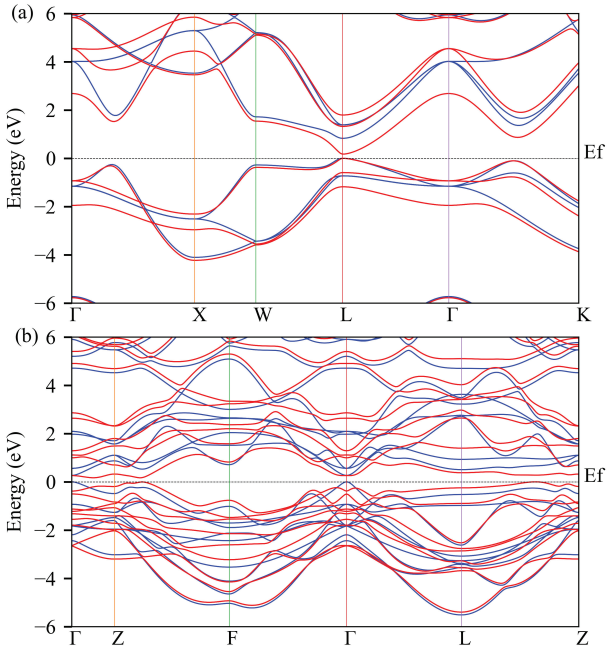

Figure 2 Calculated electronic band structures of PbTe (a), Bi_2Te_3 (b) with PBE-GGA functional. The blue lines and the red lines represent the band structures without and with SOC, respectively.

Both the valence and conduction bands of the two $Pb_2Bi_2Te_5$ stacking sequences have mixed contributions from Pb-Te and Bi-Te states belonging from different electrons states as shown in Figure 4. The DOS of the stacking B is more closely related to that of PbTe than that of Bi_2Te_3 with a strong Pb 6s state below the Fermi level, while the DOS of stacking A is more similar to that of Bi_2Te_3. The strong peak near -0.4 eV comes from the hybridization between Pb-6s, Pb-6p, Bi-6s and Te-5p for stacking A, and from a strong hybridization of Pb-6s, Bi-6s, Bi-6p and Te-5p for stacking B. In the stacking A where Pb atoms locate near the slab edge, an additional peak occurs at about -0.23 eV from a strong hybridization of Bi-6p, Pb-6p and Te-5p, especially with Te3 located at the edge of the ennead atoms slab. These results show that the inner atoms of the slab are the main contributors to the electronic band structure, the contribution of the atoms located at the edge of the slab being larger around the Fermi level. For stacking B, the tellurium atom at the slab edge (Te3) contributes less to the states near the top of the valence band due to the large electronegativity of the Bi atom to which it is bonded.

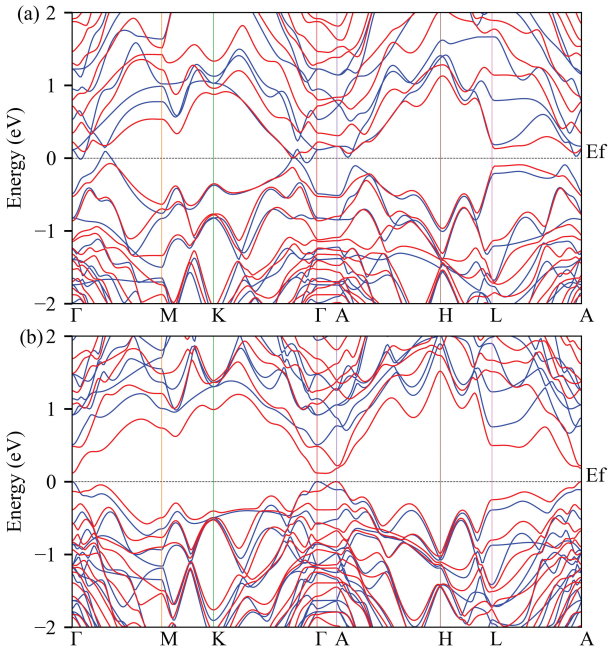

Figure 3 Calculated electronic band structures of $Pb_2Bi_2Te_5$ stacking A (a) and $Pb_2Bi_2Te_5$ stacking B (b) with PBE-GGA functional. The blue lines and the red lines represent the band structures without and with SOC, respectively.

4.2.2 Electronic transport properties

The electronic conductivity (σ) and the electronic thermal conductivity (κ_e) calculated by BolzTrap2 are given as the ratios σ/τ and κ/τ, respectively. The relaxation time τ depends on the charge carrier concentration, the temperature and the electrons energy. However, treating τ as a constant is not a satisfactory approximation to get thermoelectric properties. According to Ref[28], τ can be evaluated from effective mass approximation with deformation potential (DP) theory. The mean free path ℓ, the mobility μ and the relaxation time τ can be defined as:

$$\frac{1}{\ell} = \frac{m_e^2 {E_d^i}^2 k_0 T}{\pi \hbar^4 c_{ii}}$$

$$\mu = \frac{2(2\pi)^{1/2} e \hbar^4 c_{ii}}{3 m_e^{5/2} (k_0 T)^{3/2} {E_d^i}^2}$$

$$\tau = \frac{\mu m}{e}$$

where k_0 is the Boltzmann constant, c_{ii} is the lattice elastic constant, and E_d^i is the deformation potential expressed as:

$$E_d^i = \frac{\partial E}{\partial a/a_0}$$

where a_0 is the equilibrium lattice constant.

The effective mass m^* is derived from the second derivative of E along the a-axis and the c-axis direction: $m^*_{k,l} = \hbar^2/(\partial^2 E/\partial k_k k_l)$. For isotropic PbTe, only the c-axis has been considered while for the anisotropic Bi_2Te_3 and $Pb_2Bi_2Te_5$, both in-layers a-axis and cross-layers c-axis have been considered. The DP has been calculated by using seven values of lattice constant, namely the equilibrium one and six around this value chosen by step of 0.01 Å. A deep core state has been used as a reference to evaluate the absolute DP. The results are listed in Table 3.

The elastic constants of bulk PbTe, Bi_2Te_3 and $Pb_2Bi_2Te_5$ have been calculated by fitting the energy-strain curve to quadratic or sextuple polynomial, as detailed in Ref[45]. We have implemented a series of distortions on the equilibrium structure. The bulk modulus has been obtained by fitting the results with the Birch-Murnaghan equation. Based on the space group, the elastic constants of PbTe (C_{11}, C_{12}, C_{14}), Bi_2Te_3 (C_{11}, C_{12}, C_{13}, C_{14}, C_{33}, C_{44}) and $Pb_2Bi_2Te_5$ (same as with Bi_2Te_3) are listed in Table 4.

The temperature and doping dependence of the electronic properties S, σ and κ_e are shown in Fig. 5 and in Fig. 6. Since the best thermoelectric properties are obtained for semiconductors with carriers concentrations around 10^{19} carriers/cm^3,[50] the doping dependence was investigated in the domain of carriers concentration ranging from 10^{17} /cm^3 to 10^{22} /cm^3. The calculations have been performed for both electron-doping and hole-doping in in-layers a-axis (xx) and cross-layers c-axis (zz). As shown in Fig. 5, the maximum $|S|$ of stacking A appears in the area of

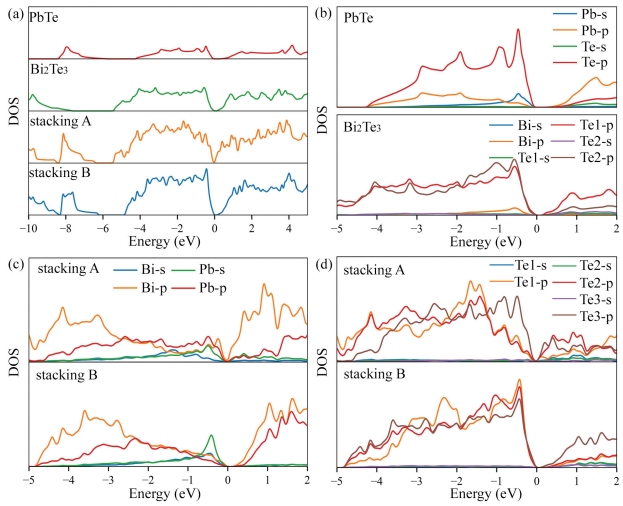

Figure 4 Total DOS (a), projected DOS of PbTe and Bi_2Te_3 (b) and projected DOS of $Pb_2Bi_2Te_5$ stacking A and B (c,d) calculated with PBE-GGA functional.

Table 3 Deformation potential constants Ed and carriers effective mass m^* at zero Kelvin in the c direction and in the ab plane calculated with PBE-GGA functional.

Structures	Charge	m^*		E_d(eV)	
		c	a,b	c	a,b
PbTe	holes	0.259		10.64	
	electrons	-0.368		9.62	
Bi_2Te_3	holes	0.123	0.018	10.73	14.05
	electrons	-0.131	-0.019	9.74	13.92
$Pb_2Bi_2Te_5$	holes	0.077	0.023	10.84	13.22
stacking A	electrons	-0.305	-0.06	8.86	12.04
$Pb_2Bi_2Te_5$	holes	1.12	0.106	9.75	12.51
stacking B	electrons	-0.343	-0.132	9.89	12.69

intermediate doping level (range 10^{19} - 3×10^{20} carriers per cubic centimeter) in a wide temperature range. Irrespective of the doping type the Seebeck coefficient absolute values are of the same order of magnitude and the anisotropy is small. By contrast to S, the in-layer σ is more than an order of magnitude larger than that in cross-layer, which is expected from the structure since the separated layer slabs along the c-axis hold together by vdW interactions. As to the stacking B in Fig. 6, the optimum doping level is relatively lower than for stacking A (around 10^{18} - 10^{19} e/cm^3). Generally, stacking B has a higher S and a lower σ than stacking A, due to the metallic character of stacking A.

4.2.3 Lattice thermal conductivity

After having comprehensively determined the electronic part of TE properties we have accurately calculated the lattice thermal conductivity κ_l of $Pb_2Bi_2Te_5$. In order to use QUANTUM ESPRESSO for this purpose we have first re-optimized the structures of PbTe, Bi_2Te_3 and $Pb_2Bi_2Te_5$ stacking A and B with this package using the PBE associated with vdW-DF2 exchange-correlation functional without SOC. The obtained equilibrium lattice constants are $a = 657$ pm for PbTe, $a = 435$ pm, $c = 2985$ pm for Bi_2Te_3, $a = 441$ pm, $c = 1752$ pm for stacking A and $a = 442$ pm, $c = 1732$ pm for stacking B, which are quite close to the constants optimized by WIEN2k and the experimental ones.

In a previous work[51] it has been reported that, van der Waals functionals yield underestimated bulk modulus by about 20-40% compared to LDA, resulting in too low phonon frequencies that do not agree with experimental data, hence these functionals have been discarded for our study. Furthermore, the harmonic phonon spectrum mostly depends on the choice of the lattice parameters and little on the choice of the functional[52]. Hence, the LDA functionals have been used to determine the harmonic and anharmonic force constants.

The longitudinal optical (LO) – transverse optical (TO) splitting at the Gamma point, which has a significant effect on the phonon dispersion of PbTe caused by large Born effective charges, has been evaluated by adding the non-analytical term to the dynamical matrix. The spectra of PbTe and Bi_2Te_3 are shown with and without LO-TO splitting in Fig. S6. A good agreement is obtained between the phonon dispersion curves of PbTe and Bi_2Te_3 along a high symmetry path and experimental data from Ref[53,54] (Fig. 7). The Born effective charges calculated by the Berry phase method[55] and dielectric constants are listed in Table 5. Because of the rock salt structure, the Born effective charge tensor of PbTe has identical diagonal elements. Furthermore, PbTe being a binary compound we have the relation $Z^*_{Pb} = -Z^*_{Te}$. The TO modes are very soft, which is well in agreement with both experimental data[54] and previous DFT

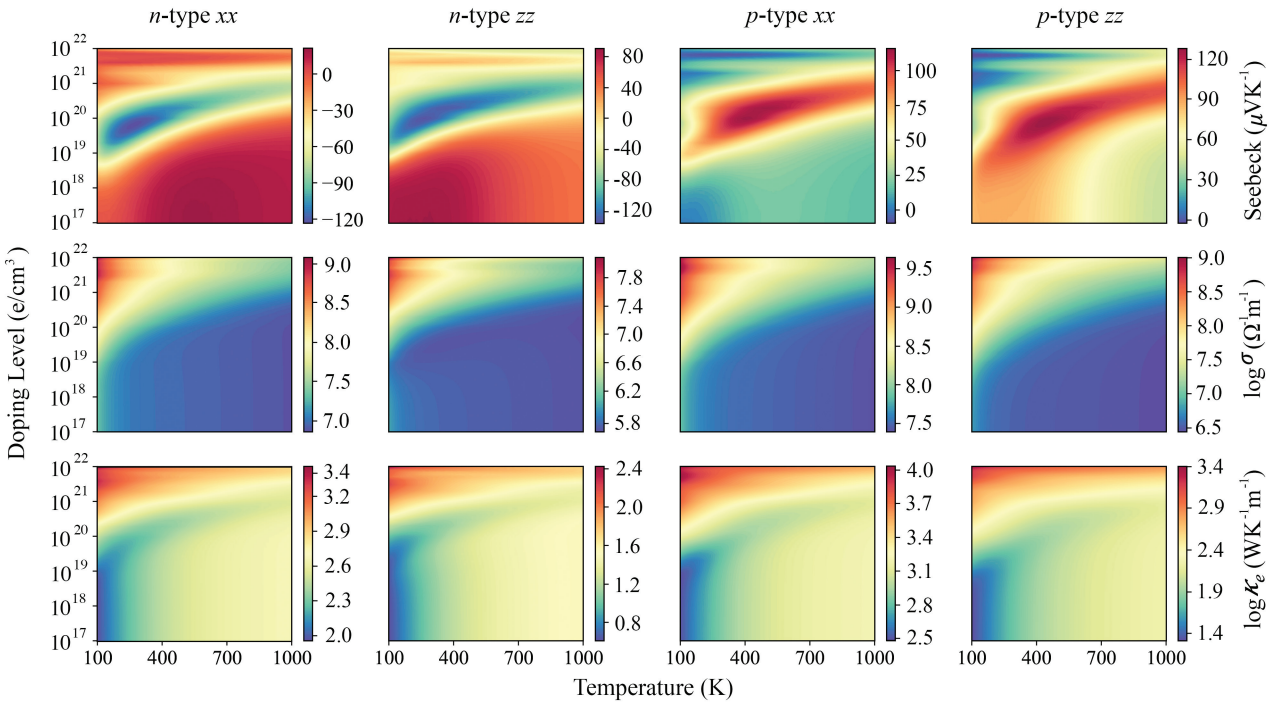

Figure 5 Calculated Seebeck coefficient, electronic conductivity and electronic thermal conductivity versus temperature and n- and p-type doping levels in in-layer a-axis (xx) and cross-layer c-axis (zz) direction for $Pb_2Bi_2Te_5$ stacking A.

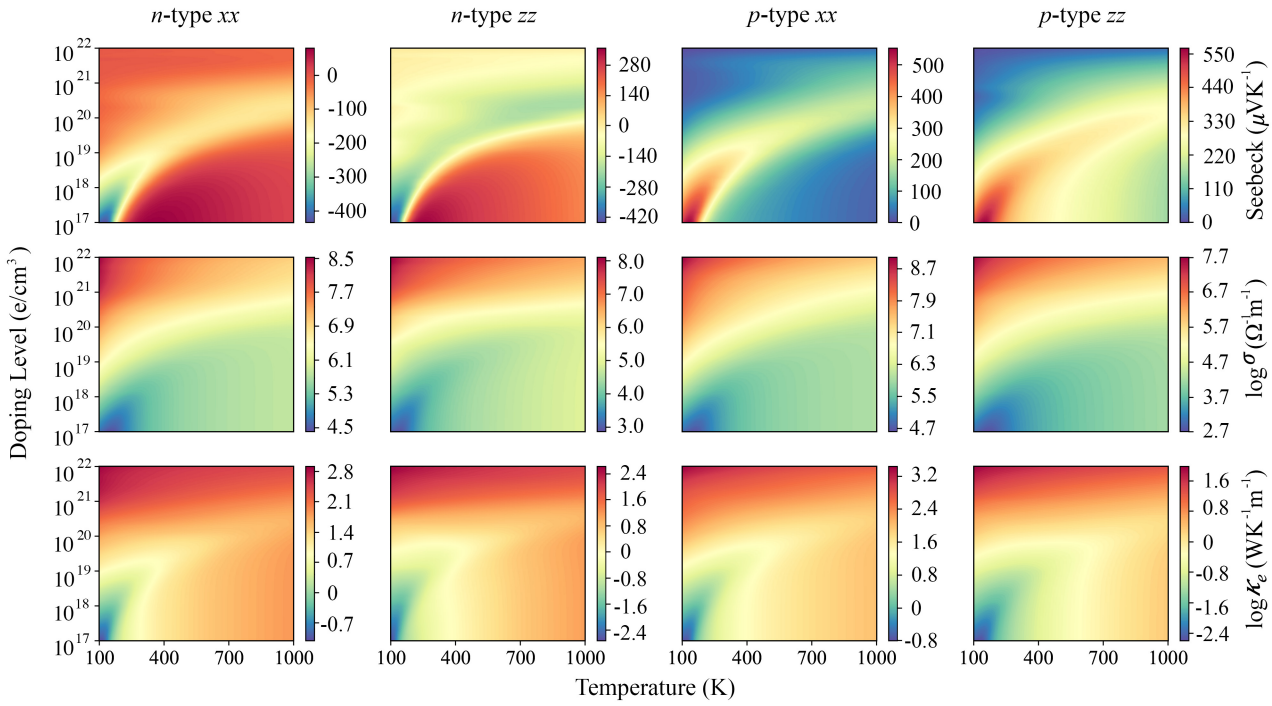

Figure 6 Calculated Seebeck coefficient, electronic conductivity and electronic thermal conductivity versus temperature and n- and p-type doping levels in in-layer a-axis (xx) and cross-layer c-axis (zz) direction for $Pb_2Bi_2Te_5$ stacking B.

Table 4 Bulk modulus B (GPa) and elastic constants C_{ij} (GPa) of PbTe, Bi_2Te_3 and $Pb_2Bi_2Te_5$ calculated with PBE-GGA together with calculated results and experimental data from the literature.

	B	C_{11}	C_{12}	C_{13}	C_{14}	C_{33}	C_{44}
PbTe	37.5	99.1	6.7	-	-	-	13.4
Other Calc.[46]	40.4	111.0	6.7	-	-	-	14.4
Exp.[47]	39.8	105.3	7.0	-	-	-	13.2
Bi_2Te_3	47.0	78.0	22.7	38.1	23.2	69.4	46.7
Other Calc.[48]	36.4	82.8	20.8	40.1	-	60.4	40.1
Exp.[49]	40.9	74.4	29.2	29.2	15.4	51.6	29.2
$Pb_2Bi_2Te_5$ stacking A	47.3	77.7	27.1	38.5	-21.1	62.4	44.1
$Pb_2Bi_2Te_5$ stacking B	45.6	77.0	21.0	37.3	-22.4	65.4	45.4

works[46,54].

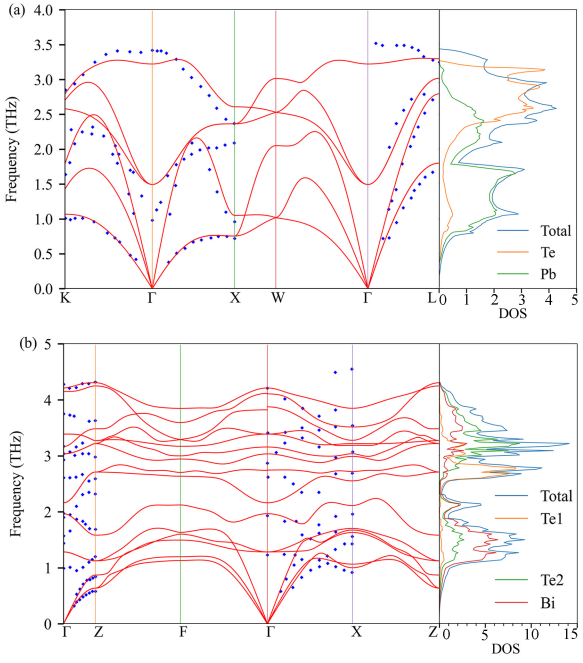

Figure 7 Phonon dispersion relations and total and projected phonon density of states for PbTe (a) and Bi_2Te_3 (b) in a unit cell at equilibrium. The solid red lines are from this work, and the blue dots are experimental results extracted from Ref[54] for PbTe and Ref[53] for Bi_2Te_3.

With the same scheme as for PbTe and Bi_2Te_3, the anharmonic force constants have been computed for $Pb_2Bi_2Te_5$. The phonon dispersion curves together with the DOS of the two stacking sequences are shown in Fig. 8. Stacking A and Bi_2Te_3 have similar dispersion curves with a unique phonon band spreading the whole Brillouin zone around 2 THz and a frequency gap between 2.3 and 2.5 THz for stacking A though being smaller for Bi_2Te_3 (2.0 to 2.1 THz). For stacking B, the bands are more interlaced than in stacking A and there is no frequency gap.

The phonon spectra similarities with Bi_2Te_3 have already been observed in literature for other layered Pb-Bi-Te compounds, namely $PbBi_2Te_4$ and $PbBi_4Te_7$.[22] Interestingly in $PbBi_2Te_4$, like in $Pb_2Bi_2Te_5$ stacking B, the Bi atoms are located at the boundary of the constitutive layers and the small peak observed at 131 cm^{-1} in the experimental Raman spectrum of $PbBi_2Te_4$ could correspond to the 4 THz frequencies of the $Pb_2Bi_2Te_5$ phonon spectrum calculated in this work (Figure 8). Indeed according to Mal et al.[22], the peak at 131 cm^{-1} is related to the interactions at the boundary of the layers and in the present work the atomic contributions to the 4 THz frequencies for $Pb_2Bi_2Te_5$ stacking B solely belong to the Bi and Te3 atoms.

To evaluate the lattice thermal conductivity κ_l, the Boltzmann transport equation (BTE)[62] has to be solved self consistently including all the scattering processes. The compounds of interest are considered as ideal ones without scattering impurities. The κ_l can be calculated using a full solution of the linearized phonon Boltzmann equation (LBTE) following the method introduced in Ref[63]. The LBTE gives a rigorous way to evaluate lattice thermal conductivity by considering phonon-phonon interactions but necessitates huge calculations. In previous researches on metal and semiconductor[64,65] the single-mode relaxation time approximation (RTA)[66] has been proved to be a fast

Table 5 Calculated Born effective charges Z^* (e) and dielectric constants ε_∞ in in-layer a-axis(xx) and in cross-layer c-axis(zz).

		This work [xx, zz]	Other works [xx, zz]
PbTe	Z^*_{Pb}	[5.75, 5.75]	[6.5, 6.5][56] [5.8, 5.8][46]
	$\varepsilon_{\infty xx}$	37.61	36.9(77 K) 32.8(300 K)[57]
Bi_2Te_3	Z^*_{Bi}	[6.83, 6.83]	[7.29, 3.58][58]
	Z^*_{Te1}	[-6.79, -6.79]	[-6.03, -5.25][58]
	Z^*_{Te2}	[-3.46, -3.46]	[-4.28, -0.96][58]
	$\varepsilon_{\infty xx}$	43.96	45-50[59–61]
	$\varepsilon_{\infty zz}$	42.36	38[60]
$Pb_2Bi_2Te_5$ stacking B	Z^*_{Bi}	[7.86, 3.93]	
	Z^*_{Pb}	[5.84, 5.98]	
	Z^*_{Te1}	[-4.41, -1.27]	
	Z^*_{Te2}	[-6.29, -5.71]	
	Z^*_{Te3}	[6.69, -5.93]	
	$\varepsilon_{\infty xx}$	54.57	
	$\varepsilon_{\infty zz}$	42.77	

Table 6 Lattice thermal conductivity (W/(m·K)) for $Pb_2Bi_2Te_5$ A and B stacking sequences obtained from LBTE and RTA at the temperatures of 300 K, 500 K, 700 K and 900 K. The average thermal conductivity values as well as that in the in-layer xx and cross-layer zz direction are given

		LBTE			RTA		
		κ_{xx}	κ_{zz}	κ_{ave}	κ_{xx}	κ_{zz}	κ_{ave}
Stacking A	300 K	0.98	0.19	0.70	0.65	0.18	0.50
	500 K	0.59	0.11	0.43	0.39	0.11	0.30
	700 K	0.42	0.08	0.31	0.28	0.08	0.21
	900 K	0.33	0.06	0.24	0.22	0.06	0.17
Stacking B	300 K	0.98	0.35	0.75	0.91	0.34	0.72
	500 K	0.59	0.21	0.46	0.55	0.20	0.43
	700 K	0.42	0.15	0.33	0.39	0.14	0.31
	900 K	0.32	0.12	0.25	0.30	0.11	0.24

and reliable choice to simplify the calculations. Within the RTA theory, the lattice thermal conductivity is given by:

$$\kappa_l = \frac{1}{NV_0}\sum_\lambda C_\lambda \upsilon_\lambda \otimes \upsilon_\lambda \tau_\lambda$$

where V_0 is the unit cell volume, υ_λ is the group velocity and τ_λ is the phonon scattering time in the specific phonon mode (λ). The summation runs over all the band in the Brillouin zone. The specific mode heat capacity of the (λ) phonon with frequency ω_λ is $C_\lambda = k_B(\hbar\omega_\lambda\beta)^2 n^0_\lambda(n^0_\lambda+1)$, with $\beta = 1/(k_BT)$. n^0_λ is the Bose-Einstein distribution function.

We have calculated the lattice thermal conductivity using both LBTE and RTA at 300 K, 500 K, 700 K and 900 K for the two stacking sequences. The results of in-layer a-axis, cross-layer c-axis, and average thermal conductivity $\kappa_{ave} = (2\times\kappa_{xx}+\kappa_{zz})/3$[67] are summarized in Table 6. With LBTE, the thermal conductivity at 300 K amounts to $\kappa_{xx} = 0.98$ $Wm^{-1}K^{-1}$ in the in-layer direction and $\kappa_{zz} = 0.35$ $Wm^{-1}K^{-1}$ in the cross-layer direction for stacking B. $Pb_2Bi_2Te_5$ with ordered sequence A has a similar κ_{xx} value to that of stacking B, while the cross-layer one κ_{zz} (0.19 $Wm^{-1}K^{-1}$) is noticeably smaller. Both structures are found to have very low and anisotropic lattice thermal conductivity. Comparing LBTE and RTA results, irrespective of the stacking, one can note that, the cross-layer κ_{zz} values are similar while the in-layer ones are different. When increasing temperature, κ_l decreases in the two directions.

The cumulative lattice thermal conductivity, phonon lifetime τ, group velocity in a-axis and c-axis directions for $Pb_2Bi_2Te_5$ with the two stacking sequences, calculated at 300 K by using RTA, are shown in Fig. 9. The temperature dependence of the thermal conductivity of the two stacking sequences in $a-$axis and c-axis directions as well as that of the average thermal conductivity are presented in Fig. 10. It can be clearly seen that the in-layers thermal conductivities of the two stacking sequences are close, while the cross-layers thermal conductivities of stacking B is almost twice as large as that of stacking A. The interaction between the acoustic branches and the optical ones plays an important role in the lattice thermal conductivities. Based on the cumulative κ_l curves, we can divide the frequency domain into three parts: (a) 0–1.8 THz, (b) 1.8–3.4 THz and (c) 3.4–4.1 THz. In the first part (a), the cumulative κ_l curves of both structures show a S-shape like behavior. In this frequency domain the cumulative lattice thermal conductivities of the two stacking sequences are similar. In the second part (b), correlated with the phonon band gap observed between 2.3 to 2.5 THz in stacking A (Fig. 8), the cumulative κ_l of this stacking sequence reaches a plateau. In the third part (c) the optical phonons come into play and participate, though weakly, to the heat conduction. The contribution provided by the first, second and third parts to heat conduction amounts to 78%, 10%, 12% for stacking

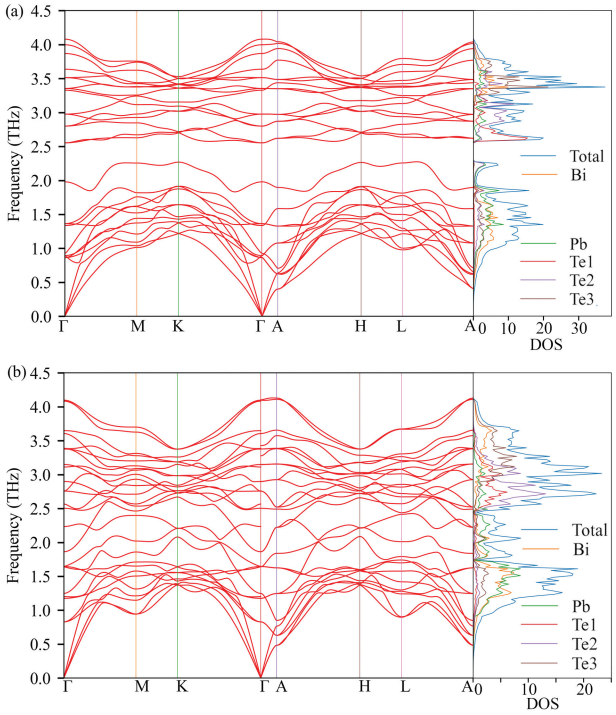

Figure 8 Phonon dispersion relations of $Pb_2Bi_2Te_5$ for stacking A (a) and stacking B (b), as well as total and projected phonon density of states.

A and 66%, 28%, 6% for stacking B, respectively. Meanwhile, the gap in the optical branches in stacking A leads to fewer phonon scattering, producing much longer phonon lifetimes (Fig. 9b).

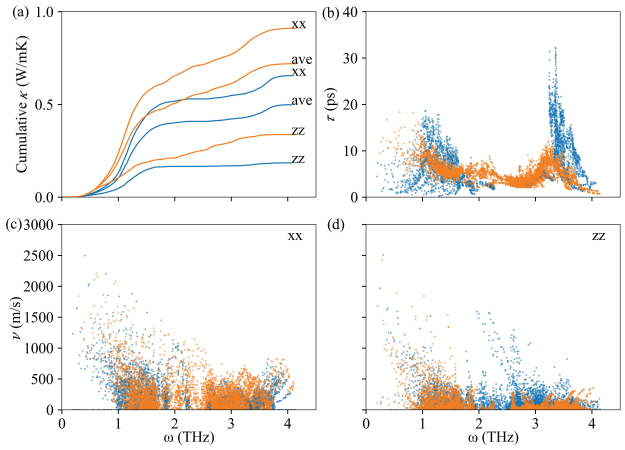

Figure 9 Calculated cumulative lattice thermal conductivity for $Pb_2Bi_2Te_5$ stacking A (blue) and stacking B (orange) with RTA (a). Phonon lifetimes for A and B (b). Group velocity for A (c) and B (d) in the in-layer a-axis and cross-layers c-axis. Results obtained at 300 K.

4.2.4 Thermoelectric figure of merit

From the Seebeck coefficients and the electronic and thermal conductivities the figure of merit zT can be evaluated as a function of carriers concentration and temperature. The results are depicted in Fig. 11,12. The zT values of $Pb_2Bi_2Te_5$ with stacking A depend little on the considered direction and carriers types. By contrast, for stacking B the zT values are much higher for p-type carriers that for n-type ones. The conditions to obtain the maximum zT are 200–300 K and $1 \times 10^{18} - 5 \times 10^{19}$ h/cm^3 along the a-axis direction, and 600–1000 K and $1 \times 10^{20} - 5 \times 10^{21}$ h/cm^3 along the c-axis one. The highest value in the a-axis direction is 4.02 and that in the c-axis direction is 2.26, which are higher than those already reported in literature for other layered chalcogenide compounds (e.g. 1.3 for the Sb_2Te_3-GeTe compounds[68], 1.4 for the Bi_2Te_3-GeTe ones[69] and 1.86 for $Bi_{0.5}Sb_{1.5}Te_3$ [70]). Despite the lower lattice thermal conductivity of stacking A, its electronic thermal conductivity is much higher than that of stacking B as a result of the metallicity (Figure 5 and 6).

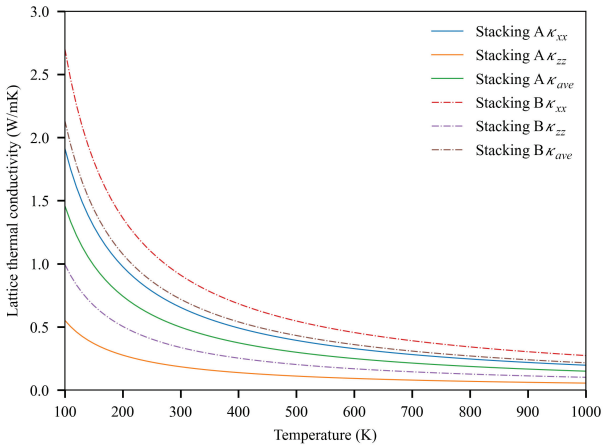

Figure 10 Calculated lattice thermal conductivity κ of $Pb_2Bi_2Te_5$ stacking A (a) and stacking B (b) vs. temperature. The evolution is plotted for the in-layer a-axis, cross-layers c-axis and average lattice thermal conductivity.

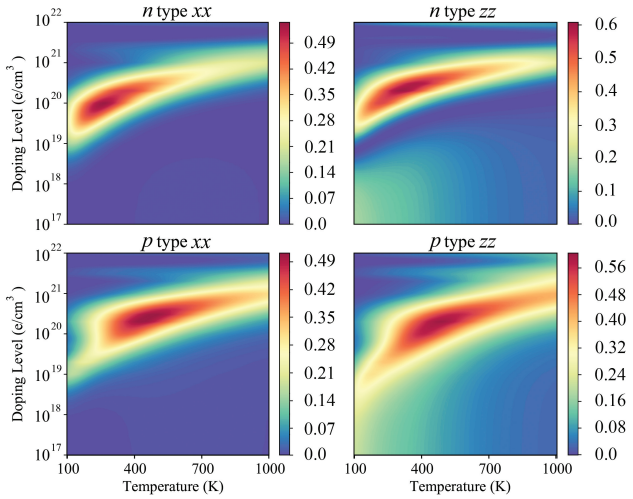

Figure 11 Calculated figure of merit zT of $Pb_2Bi_2Te_5$ stacking A in a-axis(xx) and c-axis(zz) directions vs. temperature and carriers concentration.

4.2.5 Summary of the electronic properties for both stackings of $Pb_2Bi_2Te_5$

We have gathered in Table 7 the electronic properties of stacking A and stacking B of $Pb_2Bi_2Te_5$ at low and high temperatures of 300 K and 800 K with p- and n-type doping of 10^{19} cm^{-3} and 10^{20} cm^{-3}, respectively. All the properties are reported for the xx and zz directions to highlight the anisotropy of the compounds.

The best zT values are obtained for the stacking B of $Pb_2Bi_2Te_5$ for p-type doping. This is correlated with a correspondingly high Seebeck coefficient and moderate electronic conductivity. Although the moderate electronic conductivity may be detrimental to the power factor $S^2\sigma$ appearing in the zT expression, this implies a low electronic thermal conductivity. Combined with a fairly low lattice thermal conductivity, especially in the zz direction, the figure of merit of stacking B $Pb_2Bi_2Te_5$ is improved compared to that of stacking A. Regarding stacking A, its metallic character leads to a too low Seebeck coefficient and too high electronic thermal conductivity that are not compensated by the indeed very low lattice thermal conductivity.

Due to both a thermal conductivity lying in the range of what is generally observed for glassy compounds and an electronic conductivity and a Seebeck coefficient typical of moderately doped semi-conductors, we can say that $Pb_2Bi_2Te_5$ stacking B meets the "phonon-glass, electron-crystal" (PGEC) concept.

4.3 Mechanical, dynamical and relative stabilities of stacking A and stacking B $Pb_2Bi_2Te_5$

The elastic constants that have been calculated in section 4.2.2 for permitting the determination of τ are also useful results (Table 4) to evaluate the mechanical stability of structures. The necessary and sufficient conditions of stability for the rhombohedral I system are given as[71]:

$$C_{11} > |C_{12}|;\ C_{44} > 0$$

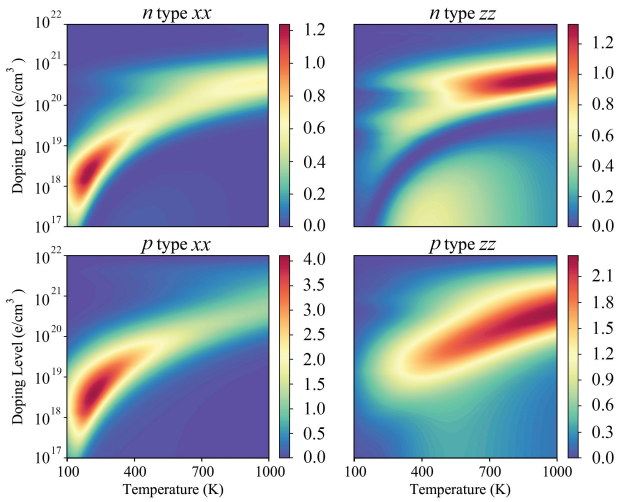

Figure 12 Calculated figure of merit zT of $Pb_2Bi_2Te_5$ stacking B in a-axis(xx) and c-axis(zz) directions vs. temperature and carriers concentration.

Table 7 Electronic properties for $Pb_2Bi_2Te_5$, stacking A and stacking B at 300 K and at a carrier concentration of 10^{19} cm^{-3} (for both n and p). Electronic conductivity $\sigma \times 10^{-5}$ in Ω^{-1}m^{-1} , electronic thermal conductivity in WK^{-1}m^{-1}, Seebeck coefficient in μVK^{-1} , lattice thermal conductivity in WK^{-1}m^{-1}.

		Electronic properties at 300 K and at a carrier concentration of 10^{19}cm^{-3}								
		σ_{xx}	σ_{zz}	κ^e_{xx}	κ^e_z	S_{xx}	S_{zz}	κ^l_{xx}	κ^l_{zz}	zT
stacking A	n-type	106	5.73	216	12.2	-31.7	54.2	0.65	0.65	0.0001
	p-type	393	40.1	715	56.6	49.9	108			0.08
stacking B	n-type	6.71	0.202	4.98	0.28	-161	-171	0.91	0.34	0.88
	p-type	11.4	0.154	7.46	0.10	296	312			3.63
		Electronic properties at 800 K and at a carrier concentration of 10^{20}cm^{-3}								
		σ_{xx}	σ_{zz}	κ^e_{xx}	κ^e_z	S_{xx}	S_{zz}	κ^l_{xx}	κ^l_{zz}	zT
stacking A	n-type	86.2	5.37	414	30.2	-24.6	2.44	0.24	0.07	0.004
	p-type	315	32.9	1429	146	56.8	87.5			0.08
stacking B	n-type	9.69	0.729	34.75	5.68	-138	-175	0.91	0.34	0.48
	p-type	13.8	0.274	53.9	0.90	206	298			1.15

$$C_{13}^2 < \frac{1}{2}C_{33}(C_{11}+C_{12})$$

$$C_{14}^2 < \frac{1}{2}C_{44}(C_{11}-C_{12}) = C_{44}C_{66}$$

whereas for cubic one they are:

$$C_{11}-C_{12}>0;\ C_{11}+C_{12}>0;\ C_{44}>0$$

In view of these mechanical stability conditions, both the two $Pb_2Bi_2Te_5$ stacking sequences are mechanically stable. This result is supported by the negative value of the cohesive energy at zero Kelvin for both stacking. The cohesion energies have been determined with the general formula:

$$E_{\text{coh}} = E_{\text{T}} - \sum_i E_i$$

where E_{T} is the total energy of the compound of interest, and E_i is the energy of the constitutive atom. The cohesive energies are -2.49 eV/at. for stacking A and -2.54 eV/at. for stacking B.

The phonon dispersion curves (section 4.2.3) provide a hint towards the dynamical stability of structures. The positive phonon values (Figure 8) in the whole Brillouin zone show that there is no dynamical instability for both stacking A and stacking B.

In agreement with literature results (see Introduction), we have found that both stacking A and stacking B can exist, however under given temperature and pressure only one of these should be stable, the other one being metastable. To investigate the relative stability of the two stacking, the Helmoltz free energy has been calculated. According to

Wang et al.[72], the free energy of a crystalline material $F(T)$, when neglecting the configurational contribution, can be expressed as follows :

$$F(T) = E_{0K} + F_{vib} + F_{el}$$

Where E_{0K} is the energy at zero Kelvin, F_{vib} is the vibrational free energy and F_{el} is the electronic free energy. The vibrational free energy reads[73]:

$$F_{vib} = \frac{1}{2}\sum_{k,\nu}\hbar\omega(k,\nu) + k_B T \sum_{k,\nu}\ln\left(1-\exp\left(\frac{\hbar\omega(k,\nu)}{k_B T}\right)\right)$$

and the electronic free energy is defined as[74]

$$F_{el} = E_{el} - TS_{el}$$

with

$$E_{el} = \int n(\varepsilon) f \varepsilon d\varepsilon + \int n(\varepsilon)\varepsilon d\varepsilon$$

and

$$S_{el} = -k_B \int n(\varepsilon)\left[f\ln(f) + (1-f)\ln(1-f)\right]$$

T, k_B , $\hbar$, f and ε are the temperature, Boltzmann constant, reduced Planck constant, Fermi-Dirac function and electrons energies, respectively. $\omega(k,\nu)$ is the phonon frequency of the k^{th} band and ν^{th} vector. The Helmoltz free energy of both $Pb_2Bi_2Te_5$ stacking is depicted in Figure 13 as a function of the temperature. Negative free energy is found for both stacking from 0 K to 1000 K and the free energy of stacking B is found to be lower than that of stacking A, suggesting that stacking B is the stable form of $Pb_2Bi_2Te_5$ whereas stacking A is the metastable one.

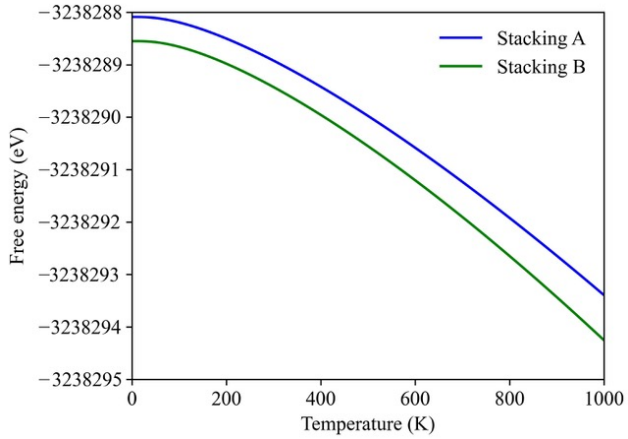

Figure 13 Helmholtz free energy per unit cell versus temperature for stacking A and stacking B of $Pb_2Bi_2Te_5$.

4.4 Electron charge density and chemical bonding

Electron charge density value and distribution play an important role in bonding trend, which will affect the thermoelectric properties. Therefore, the analysis of electron charge density and chemical bonding developed by Bader[25] and following QTAIM methods[26,75] will help us understand the reason of remarkable properties difference between the two stacking sequences. The electron charge density together with the flux lines generated by $\nabla\rho$ of the two stacking sequences in (110)-plane are shown in Fig. 14a,b with all critical points (CPs) namely nuclei, bonds (b), rings (r), and cages (c). In the studied structures, all the bond critical points (BCP) of the Pb-Te and Bi-Te bonds lie closer to the lead and bismuth atoms than to the Te ones. The change of stacking sequence does not change the numbers and types of critical points. Moreover, there is no charge accumulation along the bonds in the whole plane as evidenced by the positive Laplacian values at the BCP (Table 8). The difference in scalar distribution between the two structures is illustrated in Fig. 14c. Based on the lattice parameters in Table 1, there is a small difference between atomic positions of the two stacking structures in c-axis direction. In order to compare the difference in charge density between the two stackings, we meshed the (110)-planes with the same grid in the direction [-1, 1, 0], and the same grid between each pair of adjacent atoms in the direction [0, 0, 1]. Zhang[76] found a strong positive correlation between the anisotropy in lattice thermal conductivity and the anisotropy in electron charge density. As shown in Fig. 14c, the charge difference mainly locates in the c-axis direction, which accords with the anisotropy in lattice thermal conductivity reported in Table 7.

As mentioned above and reported in Ref[77], bonds properties play an important role in thermoelectric properties. Therefore, the topological properties of bond critical points (BCPs) in Fig. 14a,b are discussed, the results of which being tabulated in Table 8, on the basis of bond path length and angle, the charge density ρ and its Laplacian, the

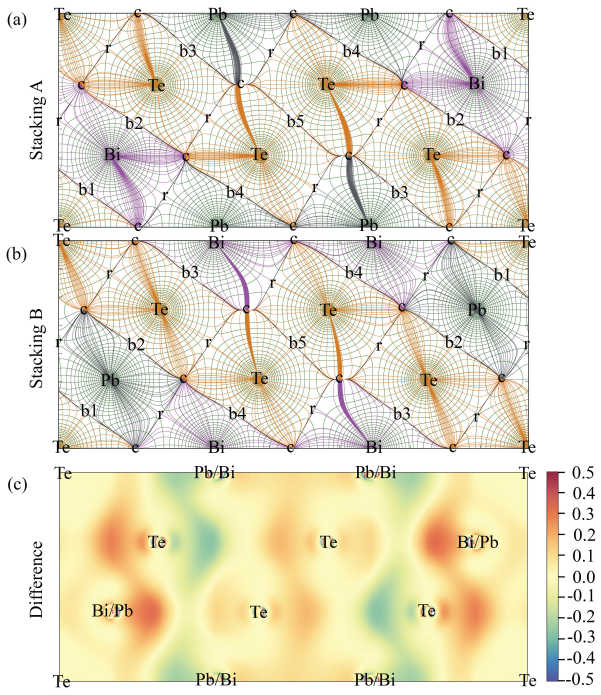

Figure 14 CPs and flux lines derived from $\nabla\rho(r)$ (light green lines) of stacking A (a) and B (b) in (110)-plane, as well as the electron charge density difference ρ_A - ρ_B (c) between the A and B stackings.

Table 8 Topological properties of $Pb_2Bi_2Te_5$ corresponding to the BCPs in Fig. 14 a, b; r1 is the distance between BCP and Bi or Pb atoms, or Te atoms for b5; r2 is the distance between BCP and Te; r1 and r2 are in unit of pm; the angle is between BCPs and their two ends; ρ and $\nabla^2\rho$ are the electron charge density and its Laplacian at the BCPs in unit of 10^{-2}e/bohr^3 and 10^{-2}e/bohr^5, respectively; G, V and H represent the kinetic, potential and total energy densities at the BCPs in unit of 10^{-2}a.u./bohr^3.

BCP	r1	r2	r1/r2	angle	ρ	$\nabla^2\rho$	G	V	H	$\mid V \mid /G$	H/ρ
A-b1	158.0	165.8	0.953	179.54	3.064	3.068	1.37	-1.98	-0.61	1.44	-1.98
A-b2	150.7	158.3	0.952	179.95	4.024	2.896	1.84	-2.95	-1.12	1.61	-2.77
A-b3	168.3	176.6	0.953	179.06	1.985	2.730	0.87	-1.06	-0.19	1.21	-0.96
A-b4	146.9	157.1	0.935	179.53	4.151	3.175	1.96	-3.12	-1.16	1.59	-2.80
A-b5	177.7	177.7	1.000	180.00	1.773	3.152	0.75	-0.90	-0.14	1.18	-0.80
B-b1	156.4	167.8	0.932	179.81	2.861	3.293	1.32	-1.81	-0.49	1.37	-1.72
B-b2	156.1	167.3	0.933	179.89	2.898	3.316	1.34	-1.85	-0.51	1.38	-1.76
B-b3	159.9	168.6	0.948	179.81	2.834	2.965	1.25	-1.76	-0.51	1.41	-1.80
B-b4	150.6	158.6	0.949	179.89	4.075	2.592	1.82	-2.99	-1.17	1.64	-2.87
B-b5	185.2	185.2	1.000	180.00	1.379	2.075	0.57	-0.63	-0.055	1.09	-0.40

bond degree (H/ρ), the kinetic energy per electron (G/ρ) and the dimensionless $\mid V \mid /G$ ratio. The electron charge density in the expected interlayer van der Waals Te-Te (b5) bondings of stacking A is much higher than that of stacking B. This lower charge density in stacking B results in a longer interatomic distance that can be explained by the higher electronegativity of Bi, which weakens the Te-Te interaction, compared to that of Pb. While within the ennead atoms slab of stacking A two poor electron density areas are found at A-b3 and A-b5 positions in Fig. 14c leading to smaller lattice thermal conductivity in c-axis direction, only one such area is found in stacking B at B-b5.

To explore the reason for the previous observations, we should catch a glimpse of bonds properties by identifying the BCPs. Usually, closed shell interactions (ionic, H-bonds and vdW) have a large positive value of $\nabla^2\rho$ over the entire interaction region, $G/\rho > 1$, $\mid V \mid /G < 1$ and a small ρ. Conversely, $\nabla^2\rho < 0$, $G/\rho < 1$, $\mid V \mid /G > 2$ and a large ρ are expected for shared interactions (covalent or polar bonds).[78]

In our study, all BCPs show small value of ρ and positive $\nabla^2\rho$ with $1 < \mid V \mid /G < 2$, which cannot be considered as pure covalent nor pure closed-shell bonds. This region has been identified by Espinosa and called a transit region[79]. In order to clearly show the tendency of BCPs, as proposed in Ref[80] the $\mid V \mid /G$ versus H/ρ plot is illustrated in Fig. 15. The Te-Te bonds of Bi_2Te_3, $Pb_2Bi_2Te_5$ stacking A and $Pb_2Bi_2Te_5$ stacking B locate in the top left area of Fig. 15, with a small magnitude of H/ρ and $\mid V \mid /G$, the latter being larger than though close to 1. The bond degree and dimensionless $\mid V \mid /G$ decrease along the sequence of $Pb_2Bi_2Te_5$ stacking A, Bi_2Te_3, $Pb_2Bi_2Te_5$ stacking B. According to Espinoza's bonding classification, these weak Te-Te bonds belong to the transit region and not to the closed shell one as would be expected for van der Waals interactions. This could be explained by the fact that the transit region

limits could be more or less displaced towards the shared shell or the closed shell regions, according to the nature of the interacting atomic pair[77].

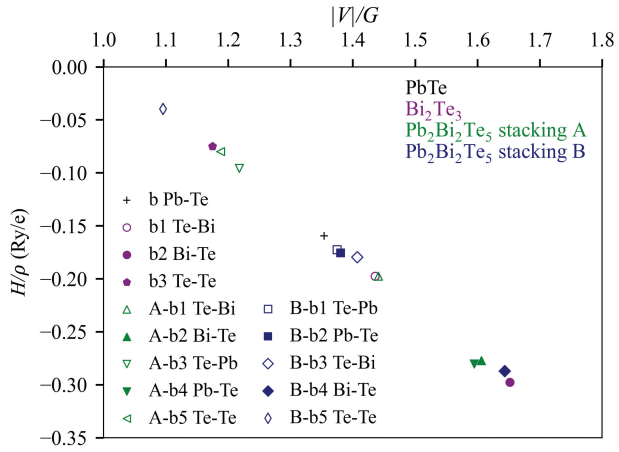

Figure 15 Dimensionless $|V|/G$ vs. bond degree H/ρ.

The electronegativity values of Pb, Bi, and Te in the Pauling scale are 1.87, 2.02 and 2.1, respectively. Hence one can assume that the ionic-like interaction and the polarity of Pb-Te are much stronger than those of Bi-Te. The BCPs properties for the binary compounds PbTe and Bi_2Te_3 are gathered in Table S1. The results show one kind of Pb-Te bond and 3 kinds of Bi-Te ones. In stacking B, the Pb-Te bonds are at the center of the slab with an approximate periodic sequence (-Te-Pb-Te-Pb-Te-) (see Fig. 1d) leading to two kinds of Pb-Te bonds and as shown in Table 8 and in Fig. 15, the properties of the two central Pb-Te BCPs (B-b1 and B-b2) are close to each other. By contrast, the properties of the two Bi-Te BCPs (B-b3 and B-b4) are different. Symmetrically in stacking A, the Bi-Te bonds are in the center of the slab but they show different central BCPs (A-b1 and A-b2) properties. The Pb-Te BCPs (A-b3 and A-b4) also differ from each other. These differences could be related to the difference in the Te-Te interaction strength, which is larger when Pb is located at the slab edge (stacking A) due to a lower electronegativity for Pb in comparison to Bi as already mentioned above. The Te atom being less electron-rich when bonded to Bi in stacking B, this induces a weaker Te-Te bond across the slabs gap, which is correlated by the larger bond length and lower absolute bond degree (Table 8). The bond distance between the Te atoms in stacking B structure (370 pm) is much smaller than the sum of the Te van der Waals radii (412 pm) suggesting that these bonds, although being weak, are not strictly of van der Waals type. This is in agreement with Gatti's[78] and Yang's[77] works that assign positive bond degree to van der Waals interactions. This difference in the Te-Te interaction strength can also explain the differences in bulk modulus values calculated above: 47.3 GPa for stacking A and 45.5 GPa for stacking B (see §4.2.2 Electronic transport properties). A lower symmetry in BCPs properties combined with stronger Te-Te interactions in stacking A should lead to a stronger anisotropy and a larger electronic conductivity in this structure. The calculated electronic properties reported in Table 7 confirm this assumption.

As mentioned above, the non-equivalent Pb-Te bonds are dissimilar in stacking A as the electron density differs from one another. One can assume that this difference originates from the position of the Pb-Te bond with respect to that of the Te-Te one. In order to check this assumption, we have built a new stacking-A-sequence structure with an increased number of layers in the slabs (21 instead of 9) and calculated, after optimisation, the topological properties of their bonds. The values are gathered in table S2. Since the structures are symmetrical, for sake of clarity we only give the properties of the non-equivalent bonds. The charge densities are plotted in Fig. 16. As expected the differences between the charge density at the critical points decrease when one move away from the Te-Te bond. In stacking B, the non-equivalent Pb-Te bonds are similar and this is also true when the number of layers in the slab is increased. However if we replace the Bi atom at the edge of the slab by a Pb one the Pb-Te bonds differentiate from one another and the difference decreases when one move away from the Te-Te bond. Therefore it seems that the Bi atom at the edge of the slab in stacking B isolates the Pb-Te bonds from the influence of the Te-Te ones between the slabs.

5 Conclusion

In this work, we have investigated the stability, the thermoelectric properties and the bonding ones of $Pb_2Bi_2Te_5$ for two stacking sequences. In agreement with experimental findings, for both stacking A and B no instability has been evidenced. In the range of temperatures 0 K-1000 K stacking B seems to be the stable form of $Pb_2Bi_2Te_5$, whereas stacking A is the metastable one. The two stacking sequences show remarkable differences in electronic properties. $Pb_2Bi_2Te_5$ with stacking B is a narrow energy gap semiconductor, with calculated indirect gap of 0.116 eV, while stacking A shows metallic character without energy gap. The thermoelectric properties of the two stacking sequences, namely the Seebeck coefficient, electronic conductivity and thermal conductivity have been calculated. To go beyond

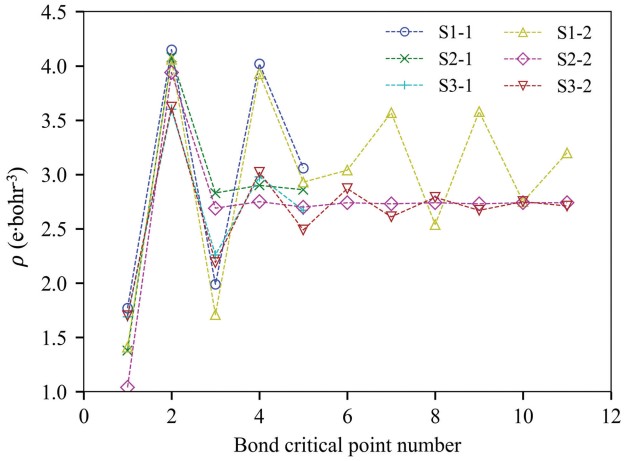

Figure 16 Electron density at the bond critical points along the slab from the edge (Te-Te interaction on the left) to the middle of the slab (on the right) in stacking-A-sequence structures with 9 (S1-1) and 21 (S1-2) layers, in stacking-B-sequence structures with 9 (S2-1) and 21 (S2-2) layers, and in stacking-B-sequence structures with the Bi atom replaced by a Pb one with 9 (S3-1) and 21 (S3-2) layers. The dashed lines are just meant to guide the eye.

the relaxation time approximation, τ has been evaluated from effective mass approximation with deformation potential (DP) theory. The calculated results show that $Pb_2Bi_2Te_5$ with stacking B has higher Seebeck coefficient, lower electronic conductivity and lower electronic thermal conductivity. Based on the calculation of phonons spectra, stacking A has stronger anisotropy and lower lattice thermal conductivity than stacking B. As a consequence, the zT values of stacking B are much higher than those of stacking A. The highest value in the a-axis direction is 4.02 and that in the c-axis direction is 2.26 with p-type carriers. The conditions of high zT are 200–300 K and 1×10^{18} - 5×10^{19} h/cm^3 in a-axis direction, and 600–1000 K and 1×10^{20} – 5×10^{21} h/cm^3 in the c-axis one.

Quantum theory of atoms in molecules (QTAIM) calculations have been performed to explore the reasons for the properties differences. The stacking sequence does not change the number or type of CPs, however, the bond Te-Te between two slabs and the Pb-Te bond near the slab edge (stacking A) are strengthened when changing the Pb atom location from the center of the slab (stacking B) to the edge (stacking A). The changing of sequence from stacking B to stacking A breaks the symmetry of the bonds strength and leads to various BCPs properties in the structure, which yield to both higher anisotropy and electronic conductivity.

Acknowledgements

The PhD thesis of Mr. W. Ma is financially supported by the China Scholarship Council (CSC). This work was granted access to the HPC resources of the Centre Informatique National de l'Enseignement Supérieur (CINES), Montpellier, France under allocation A0070806881 made by the Grand Equipement National de Calcul Intensif (GENCI). It was also granted access to the HPC resources of Aix-Marseille University financed by the project Equip@Meso (ANR-10-EQPX-29-01) of the program "Investissements d'Avenir" supervised by the Agence Nationale de la Recherche.

Notes and references

[1] M. G. Kanatzidis, *The Role of Solid State Chemistry in the Discovery of New Thermoelectric Materials, in Semiconductors and Semimetals*, Elsevier, 2001, vol. 69.

[2] L. E. Shelimova, O. G. Karpinskii and P. P. Konstantinov, *Perspekt. Mater*, 2006, 5–17.

[3] M. Saleemi, M. S. Toprak, S. Li, M. Johnsson and M. Muhammed, *Journal of Materials Chemistry*, 2011, **22**, 725–730.

[4] L. Zhang and D. J. Singh, *Physical Review B*, 2010, **81**, 245119.

[5] T. V. Quang and M. Kim, *Journal of the Korean Physical Society*, 2016, **68**, 393–397.

[6] W. Peng, D. M. Smiadak, M. G. Boehlert, S. Mather, J. B. Williams, D. T. Morelli and A. Zevalkink, *Journal of Applied Physics*, 2019, **126**, 055106.

[7] B. J. Kooi and J. T. M. De Hosson, *Journal of Applied Physics*, 2002, **92**, 3584–3590.

[8] K. Nakayama, S. Souma, C. X. Trang, D. Takane, C. Chen, J. Avila, T. Takahashi, S. Sasaki, K. Segawa, M. C. Asensio, Y. Ando and T. Sato, *Nano Letters*, 2019, **19**, 3737–3742.

[9] S. Sassi, C. Candolfi, A. Dauscher, B. Lenoir and M. M. Koza, *Physical Chemistry Chemical Physics*, 2018, **20**, 14597–14607.

[10] H. Momida, G. Bihlmayer, S. Blügel, K. Segawa, Y. Ando and T. Oguchi, *Physical Review B*, 2018, **97**, 035113.

[11] S. Barua, K. P. Rajeev and A. K. Gupta, *Journal of Physics: Condensed Matter*, 2014, **27**, 015601.

[12] T. Okuda, T. Maegawa, M. Ye, K. Shirai, T. Warashina, K. Miyamoto, K. Kuroda, M. Arita, Z. S. Aliev, I. R. Amiraslanov, M. B. Babanly, E. V. Chulkov, S. V. Eremeev, A. Kimura, H. Namatame and M. Taniguchi, *Physical Review Letters*, 2013, **111**, 206803.

[13] K. Kuroda, H. Miyahara, M. Ye, S. V. Eremeev, Y. M. Koroteev, E. E. Krasovskii, E. V. Chulkov, S. Hiramoto, C. Moriyoshi, Y. Kuroiwa, K. Miyamoto, T. Okuda, M. Arita, K. Shimada, H. Namatame, M. Taniguchi, Y. Ueda and A. Kimura, *Physical Review Letters*, 2012, **108**, 206803.

[14] J.-J. Zhou, W. Feng, Y. Zhang, S. A. Yang and Y. Yao, *Scientific Reports*, 2014, **4**, 3841.

[15] O. V. Yazyev, J. E. Moore and S. G. Louie, *Physical Review Letters*, 2010, **105**, 266806.

[16] Y. L. Chen, J. G. Analytis, J.-H. Chu, Z. K. Liu, S.-K. Mo, X. L. Qi, H. J. Zhang, D. H. Lu, X. Dai, Z. Fang, S. C. Zhang, I. R. Fisher, Z. Hussain and Z.-X. Shen, *Science*, 2009, **325**, 178–181.

[17] O. G. Karpinskii, L. E. Shelimova, E. S. Avilov, M. A. Kretova and V. S. Zemskov, *Inorganic Materials*, 2002, **38**, 17–24.

[18] P. II and I. RM, *Soviet Physics - Crystallography*, 1970, **14**, 593–596.

[19] J. W. Harrison and J. R. Hauser, *Physical Review B*, 1976, **13**, 5347–5350.

[20] A. Chatterjee and K. Biswas, *Angewandte Chemie International Edition*, 2015, **54**, 5623–5627.

[21] V. R. Sidorko, L. V. Goncharuk and B. Y. Kotur, *Ukrainskii Khimicheskii Zhurnal (Russian Edition)*, 1994, **60**, 262–265.

[22] P. Mal, G. Bera, G. R. Turpu, S. K. Srivastava, A. Gangan, B. Chakraborty, B. Das and P. Das, *Physical Chemistry Chemical Physics*, 2019, **21**, 15030–15039.

[23] L. E. Shelimova, T. E. Svechnikova, P. P. Konstantinov, O. G. Karpinskii, E. S. Avilov, M. A. Kretova and V. S. Zemskov, *Inorganic Materials*, 2007, **43**, 125–131.

[24] P. Blaha, K. Schwarz, F. Tran, R. Laskowski, G. K. H. Madsen and L. D. Marks, *The Journal of Chemical Physics*, 2020, **152**, 074101.

[25] R. F. W. Bader and H. Essén, *The Journal of Chemical Physics*, 1984, **80**, 1943–1960.

[26] A. Otero-de-la-Roza, E. R. Johnson and V. Luaña, *Computer Physics Communications*, 2014, **185**, 1007–1018.

[27] G. K. Madsen, J. Carrete and M. J. Verstraete, *Computer Physics Communications*, 2018, **231**, 140–145.

[28] J. Bardeen and W. Shockley, *Physical Review*, 1950, **80**, 72–80.

[29] S. Baroni, S. de Gironcoli, A. D. Corso and P. Giannozzi, *Reviews of Modern Physics*, 2001, **73**, 515–562.

[30] P. Giannozzi, S. Baroni, N. Bonini, M. Calandra, R. Car, C. Cavazzoni, D. Ceresoli, G. L. Chiarotti, m. Cococcioni, I. Dabo, A. D. Corso, S. Fabris, G. Fratesi, S. de Gironcoli, R. Gebauer, U. Gerstmann, C. Gougoussis, A. Kokalj, M. Lazzeri, L. Martin-Samos, N. Marzari, F. Mauri, R. Mazzarello, S. Paolini, A. Pasquarello, L. Paulatto, C. Sbraccia, S. Scandolo, G. Sclauzero, A. P. Seitsonen, A. Smogunov, P. Umari and R. M. Wentzcovitch, *Journal of Physics: Condensed Matter*, 2009, **21**, 395502.

[31] A. Togo, L. Chaput and I. Tanaka, *Physical Review B*, 2015, **91**, 094306.

[32] M. Sato, N. Iehisa and N. Karube, *International Society for Optics and Photonics*, 2000, **3889**, 208–215.

[33] J. Perdew and Y. Wang, *Physical review B*, 1992, **45**, 13244.

[34] W. Kohn and L. J. Sham, *Physical Review*, 1965, **140**, A1133–A1138.

[35] J. P. Perdew, K. Burke and M. Ernzerhof, *Physical Review Letters*, 1996, **77**, 3865–3868.

[36] I. Hamada, *Physical Review B*, 2014, **89**, 121103.

[37] F. Tran, L. Kalantari, B. Traoré, X. Rocquefelte and P. Blaha, *Physical Review Materials*, 2019, **3**, 063602.

[38] Y.-L. Pei and Y. Liu, *Journal of Alloys and Compounds*, 2012, **514**, 40–44.

[39] M. H. Francombe, *British Journal of Applied Physics*, 1958, **9**, 415–417.

[40] E. Engel and S. H. Vosko, *Physical Review B*, 1993, **47**, 13164–13174.

[41] F. Tran and P. Blaha, *Physical Review Letters*, 2009, **102**, 226401.

[42] A. Goyal, P. Gorai, E. S. Toberer and V. Stevanovic, *npj Computational Materials*, 2017, **3**, 42.

[43] W. H. Strehlow and E. L. Cook, *Journal of Physical and Chemical Reference Data*, 1973, **2**, 163–200.

[44] S. Park and B. Ryu, *Journal of The Korean Physical Society*, 2016, **69**, 1683–1687.

[45] R. Golesorkhtabar, P. Pavone, J. Spitaler, P. Puschnig and C. Draxl, *Computer Physics Communications*, 2013, **184**, 1861–1873.

[46] Y. Zhang, X. Ke, C. Chen, J. Yang and P. R. C. Kent, *Physical review B*, 2009, **80**, 1–12.

[47] A. J. Miller, G. A. Saunders and Y. K. Yogurtcu, *Journal of Physics C: Solid State Physics*, 1981, **14**, 1569–1584.

[48] Z. Xiong, *Journal of Alloys and Compounds*, 2014, **582**, 392–398.

[49] J. O. Jenkins, J. A. Rayne and R. W. Ure, *Physical Review B*, 1972, **5**, 3171–3184.

[50] A. F. Ioffe, *Semiconductors Thermoelement and Thermoelectric Cooling*, Infosearch, 1957, p. 100.

[51] O. Hellman and D. A. Broido, *Physical Review B*, 2014, **90**, 134309.

[52] D. Campi, L. Paulatto, G. Fugallo, F. Mauri and M. Bernasconi, *Physical Review B*, 2017, **95**, 024311.

[53] W. Kullmann, G. Eichhorn, H. Rauh, R. Geick, G. Eckold and U. Steigenberger, *Physica Status Solidi (b)*, 1990, **162**, 125–140.

[54] Z. Tian, J. Garg, K. Esfarjani, T. Shiga, J. Shiomi and G. Chen, *Physical Review B*, 2012, **85**, 184303.

[55] R. King-Smith and D. Vanderbilt, *Physical Review B*, 1993, **47**, 1651–1654.

[56] N. M. Ravindra and V. K. Srivastava, *Physica Status Solidi (a)*, 1980, **58**, 311–316.

[57] D. Richard, *Solid State Physics*, 1974, **28**, 179–224.

[58] S.-K. Feng, S.-M. Li and H.-Z. Fu, *Chinese Physics B*, 2014, **23**, 086301.

[59] W. Richter and C. R. Becker, *Physica Status Solidi (b)*, 1977, **84**, 619–628.

[60] H. Rahnamaye Aliabad and M. Kheirabadi, *Physica B: Condensed Matter*, 2014, **433**, 157–164.

[61] R. Groth, *Journal of Physics and Chemistry of Solids*, 1964, **25**, 1261–1267.

[62] C. Kittel, *Introduction to Solid State Physics*, Wiley, New York, Eight edn, 2005, vol. 8.

[63] L. Chaput, A. Togo, I. Tanaka and G. Hug, *Physical Review B*, 2011, **84**, 094302.

[64] E. L. da Silva, J. M. Skelton, S. C. Parker and A. Walsh, *Physical Review B*, 2015, **91**, 144107.

[65] A. M. A. Leguy, A. R. Goñi, J. M. Frost, J. Skelton, F. Brivio, X. Rodríguez-Martínez, O. J. Weber, A. Pallipurath, M. I. Alonso, M. Campoy-Quiles, M. T. Weller, J. Nelson, A. Walsh and P. R. F. Barnes, *Physical Chemistry Chemical Physics*, 2016, **18**, 27051–27066.

[66] B. H. Armstrong, *Physical Review B*, 1985, **32**, 3381–3390.

[67] F. Yang, T. Ikeda, G. J. Snyder and C. Dames, *Journal of Applied Physics*, 2010, **108**, 034310.

[68] T. Rosenthal, M. N. Scheider, C. Stiewe, M. Doblinger and O. Oeckler, *Chemistry of Materials*, 2011, **23**, 4349–4356.

[69] J. N. Kim, M. Kaviany and J.-H. Shim, *Physical Review B*, 2016, **93**, 075119.

[70] H.-S. Kim, S. I. Kim, K. H. Lee, S. W. Kim and G. J. Snyder, *Physica Status Solidi B*, 2017, **254**, 1600103.

[71] F. Mouhat and F.-X. Coudert, *Physical Review B*, 2014, **90**, 224104.

[72] Y. Wang, Z.-K. Liu and L.-Q. Chen, *Acta Materialia*, 2004, **52**, 2665–2671.

[73] M. T. Dove, *Introduction to lattice dynamics*, Cambridge University Press, 1993.

[74] L. D. Landau and E. M. Lifshitz, *statistical physics*, Pergamon Press, Oxford, New York, 1980-81.

[75] A. Otero-de-la-Roza, M. Blanco, A. M. Pendás and V. Luaña, *Computer Physics Communications*, 2009, **180**, 157–166.

[76] J. Zhang, L. Song, M. Sist, K. Tolborg and B. B. Iversen, *Nature Communications*, 2018, **9**, 4716.

[77] H. Yang, P. Boulet and M.-C. Record, *Journal of Solid State Chemistry*, 2020, **286**, 121266.

[78] C. Gatti, *Zeitschrift für Kristallographie - Crystalline Materials*, 2005, **220**, 399–457.

[79] E. Espinosa, I. Alkorta, J. Elguero and E. Molins, *The Journal of Chemical Physics*, 2002, **117**, 5529–5542.

[80] H. Yang, P. Boulet and M.-C. Record, *Computational and Theoretical Chemistry*, 2020, **1178**, 112784.